Measurement of $\bar{\nu}_\mu$ charged-current single π^- production on hydrocarbon in the few-GeV region using MINERvA

arXiv:1906.08300v3 [hep-ex] 27 Aug 2019

Physics Department, Tufts University, Medford, Massachusetts 02155, USA
Rutgers, The State University of New Jersey, Piscataway, New Jersey 08854, USA
AMU Campus, Aligarh, Uttar Pradesh 202001, India
Department of Physics, College of William & Mary, Williamsburg, Virginia 23187, USA
Sección Física, Departamento de Ciencias, Pontificia Universidad Católica del Perú, Apartado 1761, Lima, Perú
Campus León y Campus Guanajuato, Universidad de Guanajuato, Lascurain de Retana No. 5, Colonia Centro, Guanajuato 36000, Guanajuato México.
Department of Physics, Oregon State University, Corvallis, Oregon 97331, USA
University of Rochester, Rochester, New York 14627 USA
Fermi National Accelerator Laboratory, Batavia, Illinois 60510, USA
University of Geneva, 1211 Geneva 4, Switzerland
Centro Brasileiro de Pesquisas Físicas, Rua Dr. Xavier Sigaud 150, Urca, Rio de Janeiro, Rio de Janeiro, 22290-180, Brazil
Oxford University, Department of Physics, Oxford, United Kingdom
Department of Physics and Astronomy, University of Pittsburgh, Pittsburgh, Pennsylvania 15260, USA
Northwestern University, Evanston, Illinois 60208
IISER, Mohali, Knowledge city, Sector 81, Manauli PO 140306
Departamento de Física, Universidad Técnica Federico Santa María, Avenida España 1680 Casilla 110-V, Valparaíso, Chile
Department of Physics, University of Minnesota – Duluth, Duluth, Minnesota 55812, USA
Department of Physics and Astronomy, University of Pennsylvania, Philadelphia, PA 19104
Massachusetts College of Liberal Arts, 375 Church Street, North Adams, MA 01247
University of Florida, Department of Physics, Gainesville, FL 32611
University of Wroclaw, plac Uniwersytecki 1, 50-137 Wroclaw, Poland
Universidad Nacional de Ingeniería, Apartado 31139, Lima, Perú

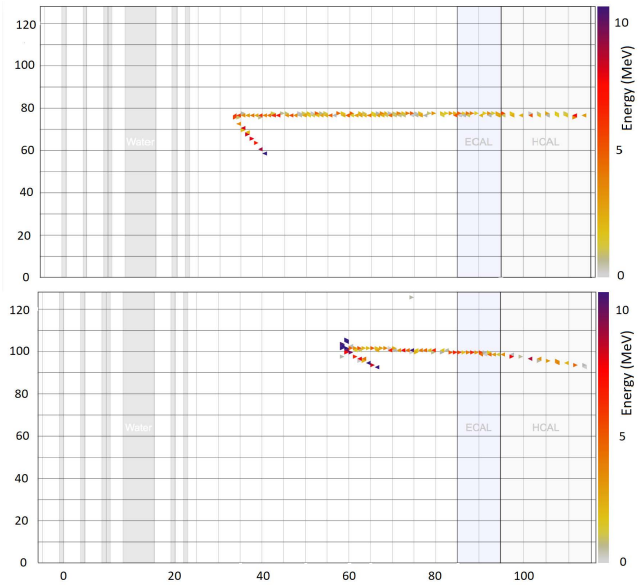
Water
ECAL
HCAL
Energy (MeV)
Water
ECAL
HCAL
Energy (MeV)

b

b

b

b

That the latter average exceeds the former reflects the rise in the signal channel cross section with increasing E_ν (see Sec. XI).

Figure 2 presents initial comparisons of the selected signal sample to reference MC predictions using distributions, prior to background subtraction, of directly-measured kinematic variables for final-state μ^+ and π^- mesons (upper, lower plots respectively). The error bands associated with the MC histograms include uncertainties associated with GENIE modeling of both signal and background processes including non-resonant pion production as described in Sec. II B. The simulation histograms give respectable descriptions of the shapes of the data distributions. For absolute event rates, however, there is a data-MC offset, with the MC prediction lying above the data in most bins. This excess rate predicted by the MC represents an 10% increase in total event rate compared to the data. (This initial excess is reduced to 8% by the background constraint of Sec. VI.) Nevertheless, the data points are mostly contained by the $\pm 1\sigma$ systematic error band of the MC prediction. The selected signal sample includes background events, mostly comprised of CC scattering into single-pion or two-pion final states that differ from channel (1). Their contribution is estimated by the reference MC and is shown by the gray-shade component histograms of Fig. 2. The overall good agreement between the data and the reference simulation at this stage is sufficient to justify its utilization by the analysis to estimate detection efficiencies and to make corrections for detector response.

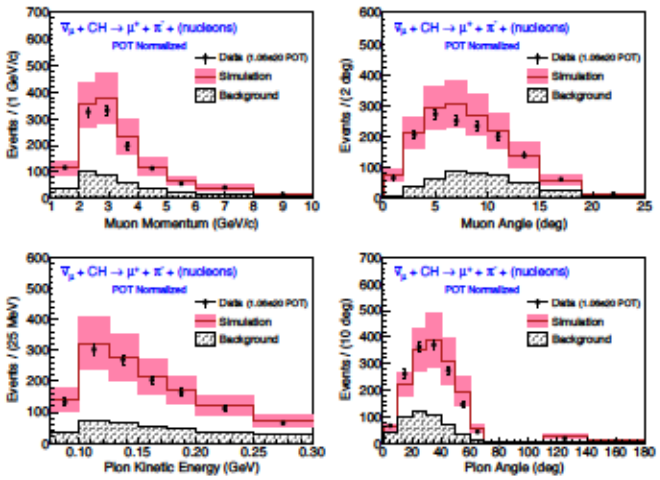

FIG. 2. Initial data distributions of the selected sample for μ^+ and π^- kinematic variables p_μ, θ_μ (upper plots) and T_π, θ_π (lower plots) compared to the reference MC predictions (histograms with systematics error band). The comparisons here are shown before constraining the background (lowermost gray-shade histogram) via sideband fitting, and prior to correcting the data for detector effects.

VI. BACKGROUND CONSTRAINT FROM SIDEBAND FITTING

The signal sample includes background processes whose final-state particle content upon exit from the target nucleus is inconsistent with channel (1). While the reference MC provides estimates for the rate and kinematic behavior of background events, these estimates come with large uncertainties. Fortunately, the estimation of background can be greatly constrained by tuning the reference MC to well-describe a background-rich "sideband sample" whose events have topological and kinematic resemblances to the selected signal events. A search for a useful sideband was carried out by inspecting samples obtained by turning off just one selection cut from the ensemble that defines the signal sample. Within the full set of cuts there are four specific ones that, when individually reversed, allow a useful sideband subsample to be defined. Then, by collecting events that pass all signal selections but one, wherein the sole rejection arises with one of the four specific cuts, a single sideband sample with discriminatory power and good statistics is obtained.

The four selection cuts are: *(i)* no reconstructed remote tracks are allowed in the event, *(ii)* all reconstructed line segments must belong to the μ^+ or π^- tracks, *(iii)* the leading hit of the pion track must lie within 6 cm of the vertex, and *(iv)* the event cannot have a Michel electron. Each data event of the sideband satisfies all signal selections but one, with the excepted selection being one of the four above-listed cuts. The sideband sample, assembled in this way, contains 4887 events.

The reference MC is amenable to a simple tuning fit to the sideband; this situation was discerned by comparing the MC predictions to data distributions of the sideband sample using the kinematic variables measured by the analysis. These include the directly measured variables of μ^+ momentum and production angle (p_μ and θ_μ), pion kinetic energy and production angle (T_π and θ_π), and the derivative variables E_ν, Q^2, and W_{exp}. The reference MC was found to describe the shapes of all seven distributions fairly well, while the absolute rate prediction was higher by $\sim$2%.

The initial comparison of the MC with sideband data is displayed in Fig. 3 which shows the sideband distributions for the kinematic variables of the μ^+ and π^- tracks. The prediction of the reference MC prior to tuning (histograms) exceeds the sideband data in the majority of bins. Approximately 75% of the sideband consists of background (lower histograms), originating mostly from CC RES or non-resonant DIS interaction categories that give rise to multi-pion final states. Importantly, the remaining $\sim$ 25% of background is estimated to be "signal contamination" as shown by the upper component histograms in Fig. 3. This component of the sideband arises with events that fail the selection criteria as the result of shortfalls in event reconstruction. Clearly, the pres-

ence of signal events in the sideband must be accounted for when fitting the reference MC to match the sideband distributions. That said, it is possible to tune the reference MC to match the sideband data distributions for all seven of the above-listed variables using the iterative procedure described below.

For sideband distributions in each of p_μ, θ_μ, T_π, θ_π, E_ν, Q^2, and W_{exp}, the distribution shapes for true background and for signal contamination are taken from the MC prediction while the absolute rate normalizations for these two components are treated as parameters in a χ^2 fit. Fitting of the MC prediction to the sideband distributions proceeds in two steps, and these are subsequently iterated. In the first step, the background normalization for the MC (a single parameter) is allowed to vary in a fit to the seven kinematic distributions of the sideband data, while the signal contamination normalization is held fixed. In the second step, a similar simultaneous fit to the kinematic distributions of the signal sample is carried out, but with the MC background estimate fixed according to the outcome of step one, while the normalization of the predicted signal content serves as the fit parameter. The revised normalizations for MC-estimated signal and background then serve as input for another two-step fitting sequence. This two-step fitting of sideband and then signal samples is repeated until the background and signal normalizations settle onto stable values. This fitting procedure converges with four iterations.

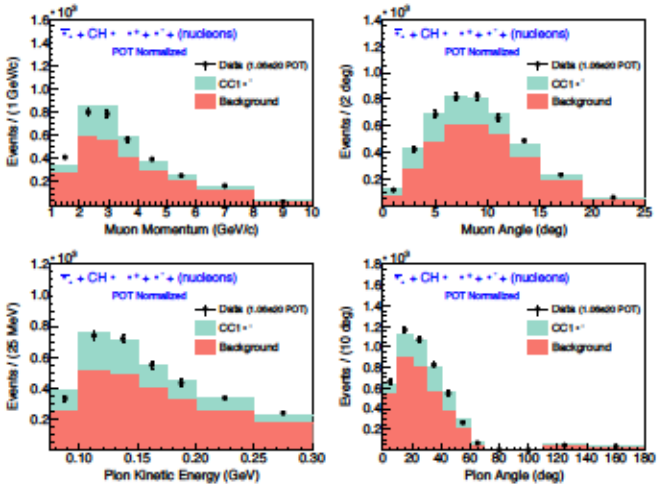

FIG. 3. Muon and charged pion kinematic distributions for sideband data events (solid points with statistical error bars) compared to the reference simulation (histograms) prior to tuning. The MC describes the shape but slightly overestimates the rate of sideband data. Lower-component histograms (red) show the estimated background content of the sideband. Upper-component histograms (green) depict the signal contamination in the sideband.

At this stage the simulation versus data was examined in each bin of the sideband distributions for all seven kinematic variable (62 bins) and the verity of predicted rate and shape was evaluated. Good agreement was observed overall. The sole exception was with three contiguous bins spanning the peak of the sideband W_{exp} distribution wherein the MC prediction was 1.2-2.5 σ higher than the data. This mild discrepancy is attributed to background events in the simulation, and weights (averaging 0.88) are assigned to MC events in the three W bins to bring the simulation closer to the data. Incorporation of these weights gives small adjustments ($\leq$ 2%) to background estimates in bins of the other kinematic variables. An uncertainty of 100% is assigned to the weights and is propagated to the final error budget.

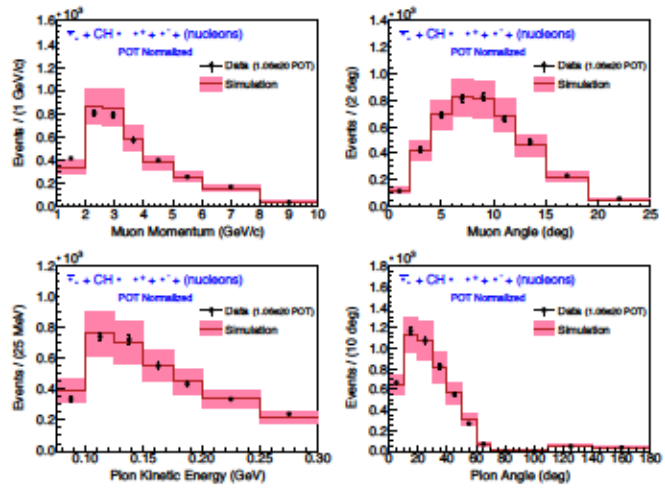

FIG. 4. Sideband sample distributions, MC versus data, for muon and pion kinematic variables (upper, lower plots respectively) prior to tuning of background and signal-contamination normalizations. The initial MC predictions and total systematic uncertainties are shown by the histograms and shaded error bands.

The result of iteratively fitting the background plus signal normalizations and tuning the predicted background W_{exp} shape is summarized in Figs. 4, 5, and 7. Figure 4 shows the sideband distributions of the directly measured muon and pion kinematic variables prior to any adjustment. The reference MC reproduces the distribution shapes quite well, with small discrepancies in absolute rate discernible in a few bins. The MC predictions, however, have significant flux and GENIE modeling uncertainties associated with them, as indicated by the shaded error bands. The sideband distributions for these same directly-measured variables after fitting and tuning, together with the derivative variables E_ν and Q^2, are shown in Fig. 5. Here, the match between data points and MC histograms is changed slightly by the fitting and tuning procedure. The main effect is that the fit constrains uncertainties associated with event-rate prediction and thus reduces the error bands of the tuned MC prediction.

Figure 6 shows the sideband distribution of the variable least directly measured, namely W_{exp}, before and

after fitting and tuning. The initial MC overprediction through the peak region $1.2 < W_{exp} < 1.5$ GeV, discernible in Fig. 6 (left), is weight-adjusted to give the improved agreement shown in Fig. 6 (right). The net change to the background normalization from the iterative fit plus shape tuning is an increase of +1%. The fit also imposes a 11% reduction in the estimated signal contamination in the sidebands.

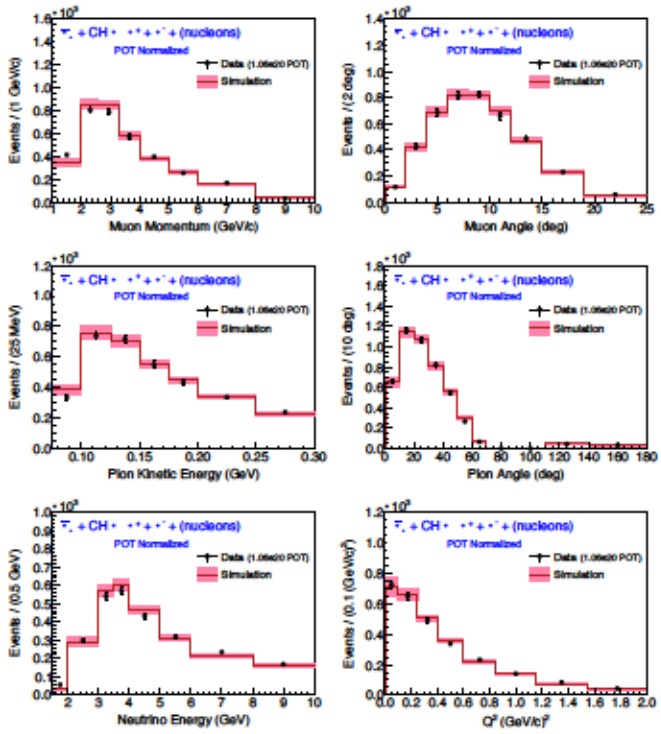

FIG. 5. Sideband distributions, MC versus data, for muon and pion variables as in Fig. 4, plus distributions for E_ν and Q^2. The MC predictions (histograms with error bands) are shown after the iterative fit of background and signal normalizations to seven kinematic distributions of the sideband and signal samples, and weight-adjusting the MC in 3 bins of W_{exp}. (see main text).

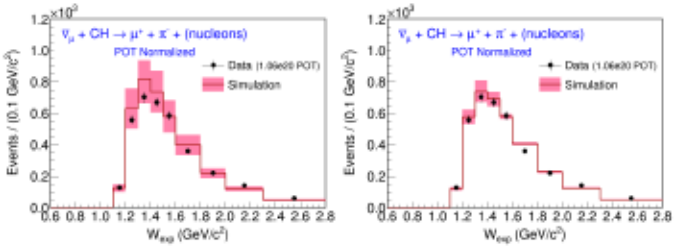

FIG. 6. Sideband distributions, MC versus data, for estimated hadronic mass W_{exp}. Left-side plot shows sideband W_{exp} prior to any adjustment of the MC. Right-side plot the improved agreement of MC (histogram with error bands) with the data after fitting of normalizations and weighting of the MC rate through the peak ($1.2 < W_{exp} < 1.5$ GeV).

After tuning the background estimate using the sideband distributions as above, the reference MC is used to predict the background contribution, N_j^{bkg}, for the jth bin of any specific distribution of signal-sample events. The true signal content is then calculated as $(N_j^{data} - N_j^{bkg})$, where N_j^{data} is the number of data candidates.

VII. DETERMINATION OF CROSS SECTIONS

Calculation of the flux-integrated differential cross section per nucleon for kinematic variable X (such as p_μ, θ_μ, and Q^2), in bins of i, proceeds as follows [10–13]:

$$(\frac{d\sigma}{dX})_i = \frac{1}{\mathcal{T}_N \Phi} \frac{1}{\Delta X_i} \frac{1}{\epsilon_i} \sum_j M_{ij}(N_j^{data} - N_j^{bkg}), \qquad (7)$$

where $\mathcal{T}_N$ is the number of target nucleons in the fiducial volume, Φ is the integrated flux, ΔX_i is the bin width, ϵ_i is the selection efficiency and acceptance. The matrix M_{ij} is the unfolding matrix [74]. It calculates the contribution to true bin i from reconstructed bin j, where the jth bin contains N_j^{data} number of data candidates and N_j^{bkg} number of background events. Calculation of $\sigma(E_\nu)_i$, the cross section per antineutrino energy bin i, is carried out using an expression that can be obtained from Eq. (7) by dropping ΔX_i and changing Φ to Φ_i, the $\bar{\nu}_\mu$ flux for the ith bin of E_ν.

The background-subtracted data is subjected to iterative unfolding [74]. The unfolding procedure takes detector resolution smearing into account and corrects reconstructed values (j) to true values (i) according to mappings, M_{ij}, determined by the reference simulation. For most of the kinematic variables measured in this work, the unfolding matrices are close to diagonal and the effects of unfolding are minor. Differences between unfolded distributions diminish rapidly with consecutive iterations and convergence was achieved within 3 iterations for p_μ, θ_μ, θ_π, and within 5 iterations for E_ν and Q^2.

Final estimation of π^- kinetic energy is an exceptional case; here the unfolding procedure introduces a significant, necessary correction. With T_π, visible track range is used to assign an initial value and it tends to give an underestimate. This is because the T_π of a negative pion, initially produced with several-tens to few-hundreds MeV, is swept through the $\Delta(1232)$ excitation region as the pion ranges out. Consequently scattering occurs at elevated rates in modes that terminate tracks (via charge exchange or absorption) and/or drain away energy via inelastic transfer to unbinding, recoiling nucleons. Track ranges thereby tend to be abbreviated, with T_π being somewhat underestimated. Consequently the unfolding procedure requires a relatively large number of iterations in order to converge to a final result. The differential cross section $d\sigma/dT_{\pi^-}$ reported in this work

(see Sec. X) is obtained using ten unfolding iterations.

For all of the above-mentioned kinematic variables including T_π, the stability of unfolded solutions was checked by unfolding ensembles of MC samples representing perturbed variations of the initial data distributions.

The bin-by-bin efficiency ϵ_i is estimated using the simulation. The selection efficiency versus muon momentum, for example, rises from 4% below 2 GeV/c and climbs to 9% at 4.0 GeV/c, as the result of improved tracking acceptance ($\theta_\mu < 25°$) for higher-momentum μ^+ tracks in the MINOS near detector. Above 6 GeV, the efficiency gradually diminishes as the result of the E_ν cut at 10 GeV. As previously stated, the overall selection efficiency for signal events is 5.8%.

The analysis uses current determinations of the integrated and differential $\bar{\nu}_\mu$ fluxes over the E_ν range 1.5 to 10 GeV for the NuMI low-energy antineutrino beam mode [40]. The $\bar{\nu}_\mu$ flux in bins of E_ν is given in the Supplement [75]. The value for the integrated flux Φ is 2.00×10^{-8} $\bar{\nu}_\mu/\mathrm{cm}^2/\mathrm{POT}$.

VIII. SYSTEMATIC UNCERTAINTIES

Cross-section measurements require knowledge of selection efficiencies, detector acceptance and resolutions, distribution shapes and normalizations of backgrounds, and the antineutrino flux. The estimation of each of these quantities introduces uncertainties. Many of the sources of uncertainty that affect the present work were encountered by previous MINERvA studies of CC(π) interactions and their treatment has been described in publications [10–13]. The systematic uncertainty from the antineutrino flux is described in detail in Refs. [40, 76].

The sources of uncertainty can be grouped into six general categories. In Figs. 7 and 8 of this Section, and in Tables of the Supplement [75], the fractional uncertainties for each bin of each measurement are decomposed using these categories. The first category, designated by "Detector", is assigned to detector response uncertainties arising from particle energy scales, particle tracking and detector composition. Categories two, three, and four include, respectively, uncertainties from simulation modeling of neutrino interactions, GENIE model uncertainties for FSI involving produced hadrons, and antineutrino flux uncertainties. These categories are designated as "X-Sec Model", "FSI Model", and "Flux". Then there are uncertainties that arise with estimation of rate and distribution shapes for the background; these are compiled in the category labeled "Bkg Est". Finally, there are statistical uncertainties that reflect finite sample sizes and the consequent uncertainties that these generate in the unfolding. These are included together in the "Statistical" category.

Systematic uncertainties are evaluated by shifting the relevant parameters in the simulation about nominal values within their $\pm1\sigma$ bands and producing a new simulated event sample. Cross sections are then recalculated using an ensemble of such alternate-reality samples, and a covariance matrix is formed from the results. The procedure is repeated for each systematic source; details are given in Ref. [12]. On cross-section plots to follow, the error bars shown represent the square roots of covariance diagonal entries. The full correlation matrices are given in the Supplement [75].

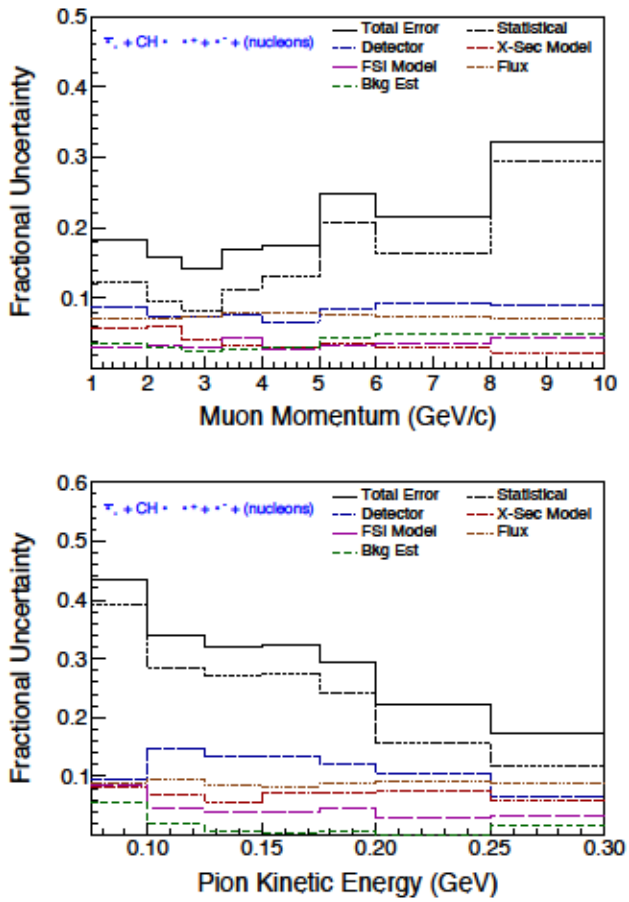

FIG. 7. Composition of fractional uncertainty in terms of systematic error categories plus the statistical uncertainty, for differential cross sections in μ^+ momentum (upper plot) and π^- kinetic energy (lower plot). The statistical uncertainty (short-dash-line histogram) is the leading error source in all bins, with detector response (fine-dash) and antineutrino flux (dot-dot-dash) uncertainties also contributing significantly.

Uncertainty decompositions representative of cross-section determinations of directly measured kinematic variables are shown in Fig. 7, for μ^+ momentum (upper plot) and for charged pion kinetic energy (lower plot). For all bins of either distribution, the finite data statistics (short-dash histogram) gives rise to larger uncertainties than does any single systematic category. In particular, the large statistical error assigned to pion kinetic energies below 200 MeV reflects a large unfolding-correction uncertainty. The detector response category contributes fractional uncertainties that range from 7%

to 9% for muon momentum, and from 6% to 15% for pion kinetic energy. Uncertainties assigned to the antineutrino flux are subject to constraints provided by the background normalization procedure. Figure 7 shows the fractional uncertainties from the flux and from the interaction cross-section model (GENIE) categories to be constant or slowly varying over the measured ranges of p_μ and T_π, with value ranges of 7% to 8% and 8% to $\leq$10% respectively.

The differential cross sections of this work include E_ν and Q^2. Since these variables are less directly related to observations than are the muon and pion, their uncertainties have compositions that differ somewhat from those shown in Fig. 7. By way of illustration, the uncertainty decomposition for E_ν is shown in Fig. 8. Here the statistical uncertainty dominates the low ($<$ 2.0 GeV) and high ($>$ 6.0 GeV) neutrino energy bins, however in the E_ν range central to this work the flux and detector response give fractional uncertainties of 9-12% and 9% respectably – values that rival or exceed the statistical error.

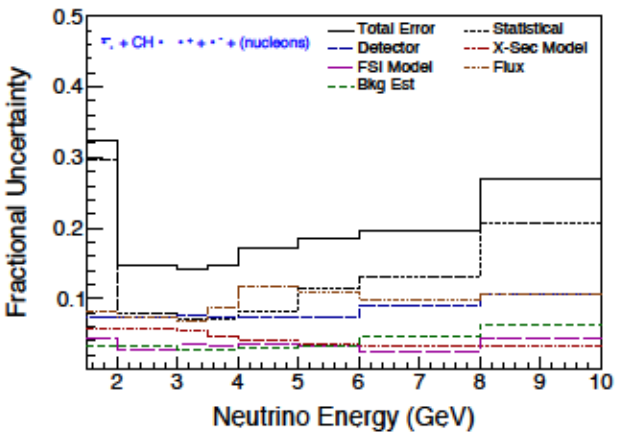

FIG. 8. Bin-by-bin fractional uncertainty in systematic error categories plus statistical uncertainty, for cross section as a function of E_ν. The flux and detector response uncertainties are comparable to the statistical uncertainty in the 2.0 to 6.0 GeV range of E_ν.

The six uncertainty categories encompass all significant systematics of the analysis, including the methodology by which nucleon kinetic energy is treated. Nevertheless, it is of interest to quantify the sensitivity of the E_ν determination to the reliance on kinematics for the inclusion of final-state nucleon T_N. For this purpose a simulation study was performed wherein an uncertainty band for T_N was assigned that covers the difference between binned values extracted by the analysis versus MC true values. Fractional uncertainties of 5%, 10%, and 25% where allotted to T_N ranges of 0-125 MeV, 125-200 MeV, and $>$ 200 MeV respectively. Simulation data for T_N was then varied randomly in accord with the error band and E_ν was recalculated. The resulting r.m.s. spread in the fractional deviation of E_ν was less than 2.0% overall, with deviations trending to higher values for $E_\nu > 5.5$ GeV. As Fig. 8 clearly shows, an uncertainty of this magnitude is well-covered by the ensemble of systematic and statistical uncertainties assigned to the E_ν measurement.

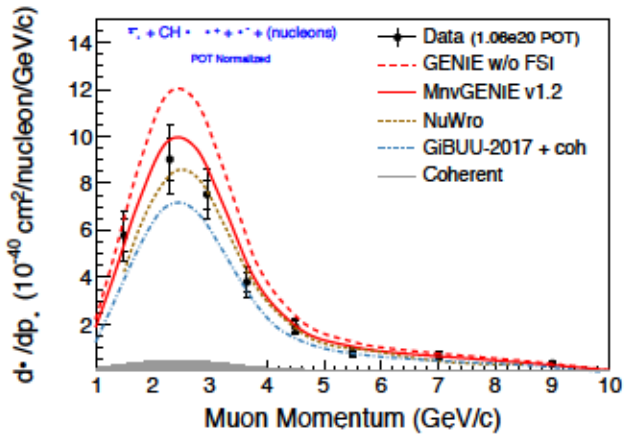

FIG. 9. The flux-integrated muon-momentum differential cross section, $d\sigma/dp_\mu$ for muons with $\theta_\mu \leq 25°$. Data (solid circles) are shown with inner (outer) error bars that denote the statistical (total) uncertainties. The solid-line (dashed) curves show GENIE predictions with (without) FSI. Short-dash and dot-dash curves show predictions by NuWro and GiBUU-2017. The estimated contribution from CC coherent scattering (4) is given by the shaded region.

IX. MUON KINEMATICS OF $\bar{\nu}_\mu$-CC(π^-)

A. Muon momentum

Figure 9 shows the differential cross section for μ^+ momentum, $d\sigma/dp_\mu$, of the signal channel. The data are shown by the solid circles in the figure, with fully (partially) extended error bars denoting the total (statistical) error associated with each data point. Included in the cross section is a small event rate from CC coherent scattering reaction (4) whose estimated contribution is indicated by the shaded area along the base of the distribution. In accordance with the analysis signal definition, this differential cross section (and all others to follow) is flux-integrated over the range 1.5 GeV $\leq E_\nu \leq$ 10 GeV, with the μ^+ direction at production restricted to $\theta_\mu \leq 25°$. The $\bar{\nu}_\mu$ flux spectrum strongly influences the shape of $d\sigma/dp_\mu$. The distribution peaks near 2.5 GeV and then falls off rapidly as p_μ increases. Predictions obtained with the GENIE-based MC are shown by the two upper-most (red) curves in Fig. 9. The dashed curve depicts a simulation in which pion and nucleon FSI effects are neglected. It differs significantly from the full reference simulation with FSI included, shown by the solid-line curve. The difference is an average event-rate reduction of nearly 20%, reflecting the strength of pion FSI in carbon, principally with π^- absorption, for pions

produced with kinetic energies in the region of $\Delta(1232)$ excitation by π^- intranuclear scattering. With inclusion of FSI, the GENIE-based simulation still lies above the data, giving an absolute event rate that exceeds the data by 8%. Allowing for the overestimate, one sees that the shape of the distribution is approximately reproduced for $p_\mu > 2$ GeV/c.

The short-dash and dot-dash curves in Fig. 9 that lie below the GENIE prediction show expectations based on the NuWro and GiBUU-2017 event generators respectively. NuWro does better than either GENIE or GiBUU-2017 with predicting the absolute data rate for most of the momentum range, with exception of momenta below 2 GeV/c where GENIE matches the observed rate while the NuWro and GiBUU-2017 predictions fall below the data. When each of the three generator predictions for this differential cross section is area-normalized to the data (not shown), the generator curves nearly coincide and all three generators give a good characterization of the distribution shape.

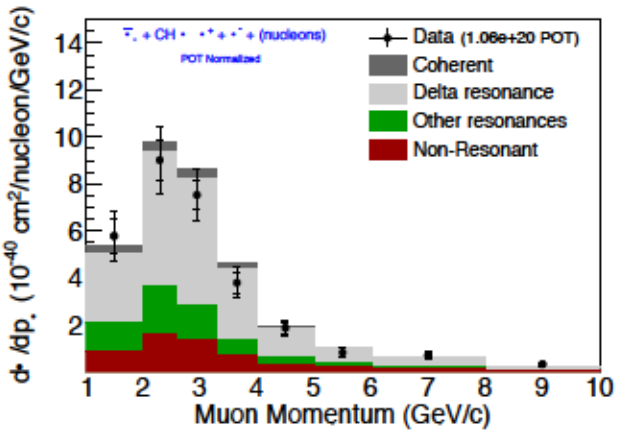

FIG. 10. Cross section $d\sigma/dp_\mu$ as in Fig. 9, compared to component reaction processes of the reference simulation. Production of $\Delta(1232)^-$ is predicted to dominate the signal channel (gray-shade histogram) in all bins of muon momentum.

The events of signal channel (1) can be characterized as originating from one of four processes: *i)* pion production via the $\Delta(1232)$ resonance, *ii)* pion production via other baryon resonances, *iii)* Non-resonant pion production including DIS reactions, and *iv)* coherent pion production via reaction (4). Figure 10 shows the relative strengths of these processes as predicted by the reference simulation. According to GENIE, Δ^- production accounts for 59% of the rate (upper, light-shade histogram in Fig. 10); production and decay of higher-mass N^* resonances gives an additional $\simeq 20\%$, with non-resonant pion production and CC coherent scattering accounting for the remaining 17% and 4% of the total rate, respectively. These rates are for final states at emergence from target nuclei, having been subjected to hadronic intranuclear scattering. Their relationship to initially-produced final states is inferred using the FSI model of the reference MC. The relationship is well-illustrated by CC non-resonant single-π^- events wherein 12.5%, 9.5%, and 1.6% portions of the initial sample migrate out of channel (1) as the result of pion absorption, pion charge exchange, and of other hadronic FSI.

The four processes listed above are broadly distributed within the muon momentum distribution. Figure 10 indicates that the rate mis-match between GENIE and data could be alleviated by reducing contribution(s) from the three non-coherent processes, but the data do not allow a unique prescription to be identified.

B. Muon production angle

Figure 11 shows the μ^+ differential cross section as a function of polar angle, θ_μ, with respect to the beam direction. The distribution peaks near 7° and then decreases gradually at larger angles.

Comparison of GENIE, NuWro, and GiBUU-2017 predictions to the data show similar trends to those noted in Fig. 9. All three generators give fairly accurate characterizations of the shape of $d\sigma/d\theta_\mu$, although the data above $\sim 6°$ exhibits a relatively flatter distribution. Readily discernible is the over-prediction of absolute rate by GENIE and its under-prediction by GiBUU-2017, with the closest agreement being achieved by NuWro. The small contribution expected from CC coherent single-pion production (shaded region in Fig. 11) is mostly confined to θ_μ into forward angles $< 10°$. The fractional contributions from the three most prominent processes displayed in Fig. 10 are predicted by GENIE to be nearly uniformly distributed over the measured angular range.

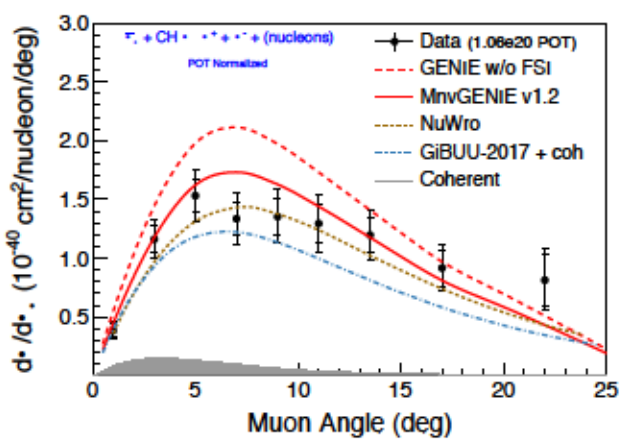

FIG. 11. Differential cross section for muon production angle, $d\sigma/d\theta_\mu$. Data (solid circles) is compared to the predictions of GENIE with and without FSI (dashed, solid uppermost curves) and with predictions from NuWro and GiBUU-2017. The distribution shape is reproduced by all generators; NuWro comes closest with predicting the absolute event rate.

The cross sections $d\sigma/dp_\mu$ and $d\sigma/d\theta_\mu$ can be compared to those previously reported by MINERvA for $\bar{\nu}_\mu$-CC($1\pi^0$) and for ν_μ-CC(π^+) and ν_μ-CC($1\pi^0$) [11, 13]. The observed spectral peaks roughly coincide for all four data sets, even though the absolute cross sections are fairly different. Differences in cross section magnitudes are certainly to be expected, since the four pion production channels differ in their isospin compositions and in the role played by interferences between vector current and axial vector current contributions, the latter being constructive in the ν_μ channels and destructive in the $\bar{\nu}_\mu$ channels.

X. PION KINEMATICS OF $\bar{\nu}_\mu$-CC(π^-)

Figure 12 shows the differential cross section for pion kinetic energy, $d\sigma/dT_{\pi^-}$. Events in the lowest T_{π^-} bin have short π^- tracks and their detection efficiency (2.8%) is 2.4 times lower than that of the next higher bin. The efficiency correction to this bin mostly removes the depletion that appears in the initial data distribution for pion kinetic energy (lower-left plot of Fig. 2). Additionally, the efficiency correction tends to flatten the remainder of the distribution. The bin-by-bin uncertainties assigned to the data points are relatively large, reflecting the fact that the kinetic energy estimation for π^- tracks receives sizable corrections from the unfolding procedure. The upper plot shows the gradually-falling shape of $d\sigma/dT_{\pi^-}$ to be reproduced by predictions from the generators, and the absolute rate is roughly described. The level of agreement provides support for the various FSI treatments for pions initiated within carbon nuclei that are invoked by GENIE, NuWro, and GiBUU.

Produced π^- mesons of the signal channel and the pions of background reactions as well can undergo absorption, elastic and inelastic scattering, and/or charge exchange as they traverse the struck nucleus. These pion FSI processes are especially prominent in range 90 MeV $< T_\pi <$ 210 MeV corresponding excitation of the Δ in π^- scattering on carbon [77]. The agreement obtained by the GENIE-based MC for $d\sigma/dT_{\pi^-}$ is notable because the prediction represents a fairly intricate prediction that involves all pion subprocesses of the FSI model.

A breakdown of contributions from the component processes is presented in the lower plot of Fig. 12. The stacked histograms indicate that pions experiencing inelastic scattering, elastic scattering, or no scattering comprise the bulk of the sample (three lowest histograms), while background feed-in from multiple-pion production with absorption and from $\pi^0 \to \pi^-$ charge exchange occurs with small rates (two uppermost histograms). These processes are in addition to the significant amounts of absorption and charge-exchange that π^- from initially produced signal events are predicted to undergo. According to the GENIE model, these latter processes have already winnowed down the signal sample from the initial interaction rate shown by the GENIE prediction without FSI (dashed curve in upper plot of Fig. 12), to give the rate predicted with FSI included – depicted by the solid curve (upper plot) and the summed histograms (lower plot) of Fig. 12. Thus reproduction of the observed π^- kinetic energy is achieved in the GENIE model by accounting for the combined effect of pion intranuclear elastic and inelastic scattering, charge exchange, absorption, together with instances of free pion propagation through target carbon nuclei.

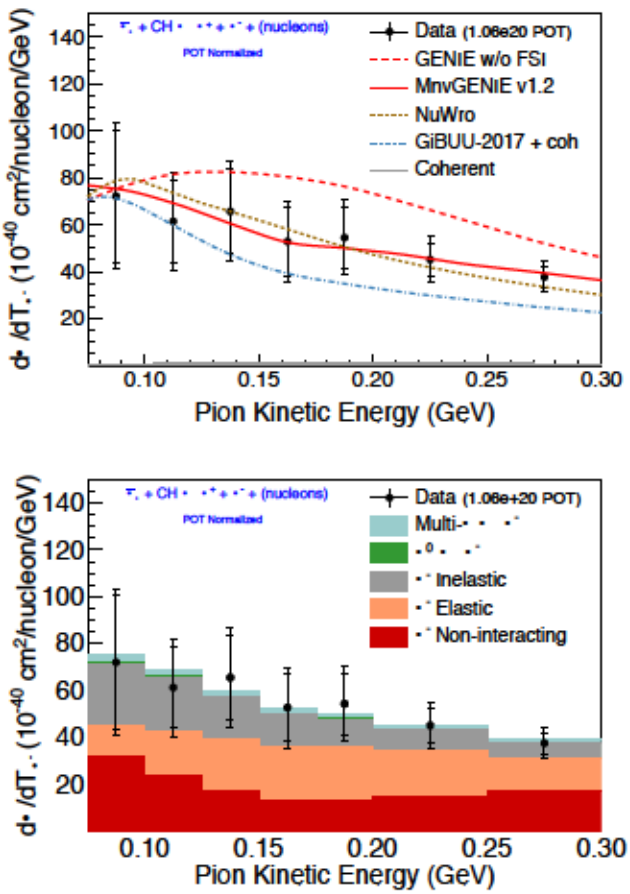

FIG. 12. Differential cross section $d\sigma/dT_{\pi^-}$ for pion kinetic energy. Upper plot compares the data (solid points) to predictions by the GENIE-based MC, NuWro, and GiBUU-2017. Lower plot shows that GENIE achieves agreement with measured $d\sigma/dT_{\pi^-}$ by combining pion FSI processes that differ in their component shapes.

Figure 13 shows the differential cross section in pion angle measured relative to the $\bar{\nu}$ beam direction. The data shows that most π^-s are produced in the forward hemisphere of the Lab frame, with angles around 30° being most probable. The upper plot shows that the regions on either side of the peak are not well-described by the event generators. The data includes occurrences of CC coherent scattering via reaction (4), and this reaction is included in all of the generator predictions displayed in the Figure. In particular, the CC coherent contribution

measured by MINERvA is shown by the gray-fill distribution in the upper plot. This contribution is included in the GENIE-based reference simulation shown by the solid curve in the upper plot. It is also included as part of the "π^- Non-interacting" component displayed in the lower plot. In the upper plot, the χ^2 per degrees of freedom for the reference simulation with (without) FSI is 24.2/11(47.8/11), while for NuWro and GiBUU-2017 it is 15.3/11 and 12.7/11 respectively.

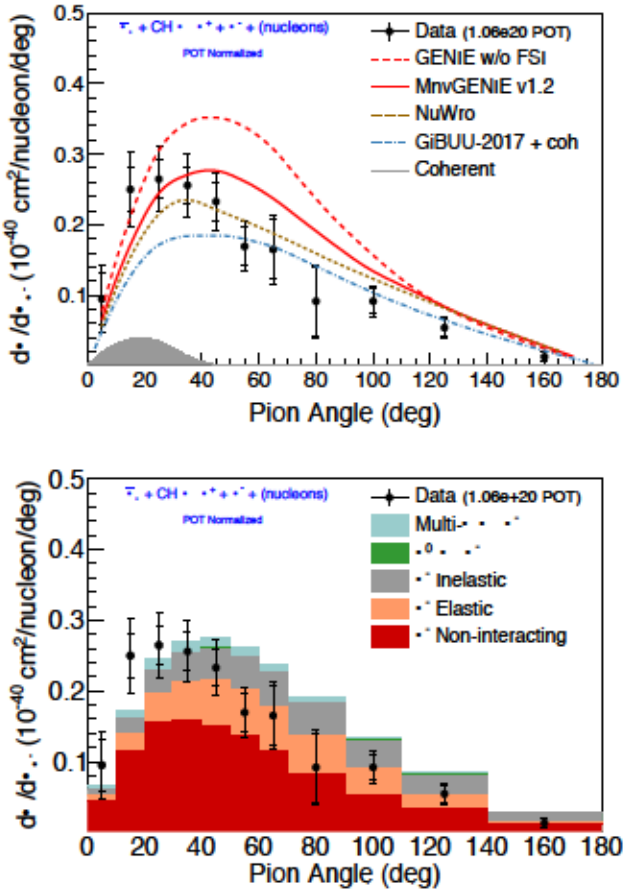

FIG. 13. Differential cross section for pion production angle. Upper plot shows the data with predictions from the GENIE-based MC and from NuWro and GiBUU-2017. The gray-fill distribution depicts CC coherent scattering as measured by MINERvA. Although coherent scattering is included in all the generator predictions, the data rate into forward $< 20°$ is underpredicted. Lower plot shows contributions to $d\sigma/d\theta_{\pi^-}$ from component pion FSI processes as estimated by the GENIE MC. Coherent scattering is included in "π^- Non-interacting".

The lower plot in Fig. 13 decomposes the GENIE prediction into pion FSI processes, with "pion non-interacting" (plus coherently produced) being included as a process. None of the component processes are predicted to have angular features that change rapidly with increasing θ_{π^-}. Modeling of the inelastic and elastic FSI contributions include prescriptions for deflections of the initial pion direction. Presumably these could be adjusted to give a better description of the data.

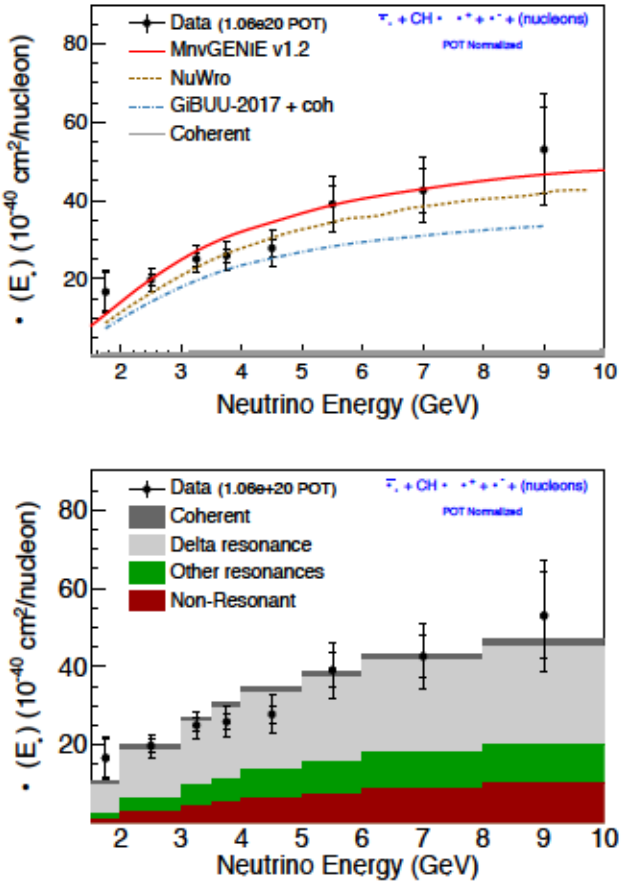

FIG. 14. Cross section (solid circles) as a function of antineutrino energy for channel (1). Upper plot compares the data to GENIE, NuWro, and GiBUU-2017 expectations. Lower plot shows contributions estimated by GENIE from coherent scattering, Δ^- resonance production, N* states above the Δ, and pion non-resonance processes.

XI. CROSS SECTIONS FOR E_ν AND Q^2

Figure 14 shows the cross section as function of antineutrino energy, $\sigma(E_\nu)$, for the signal sample, for which the invariant hadronic mass is restricted to $W_{exp} < 1.8$ GeV. The data exhibit a gradual rise from threshold that continues with increasing E_ν to the end of the measured range at 10 GeV. This behavior contrasts with the cross-section energy dependence of ν_μ-induced CC(π) wherein the slope of $\sigma(E_\nu)$ turns over and remains nearly zero above ~ 5 GeV [11, 13]. These differing trends reflect the underlying vector minus axial vector $(V - A)$ structure of the hadronic current in $\Delta S = 0$ semileptonic interactions. The VA interference terms contribute significantly to the cross sections at sub-GeV to few-GeV values of E_ν, however they diminish rapidly relative to

the $|V|^2$ and $|A|^2$ terms at higher incident (anti)neutrino energies. In contrast to ν_μ-induced CC(π) cross sections, VA interference terms are of opposite sign and destructive for $\bar{\nu}_\mu$-CC(π) interactions. Consequently the slope turn-over point for cross sections of antineutrino CC(π) channels occurs at a distinctly higher incident energy than is observed with neutrino-induced CC(π).

The three curves representing predictions based on GENIE, NuWro, and GiBUU-2017 in Fig. 14 (upper plot) exhibit the expected gradual rise of the cross section with E_ν. The GENIE-based reference MC is in agreement with the data with exception for the region between 3.5 to 5 GeV where offsets of order $1\,\sigma$ are indicated. The NuWro prediction falls below the data in the two lowest E_ν bins, but matches the data to within $1\,\sigma$ throughout the higher E_ν range. The GIBUU-2017 prediction, however, lies below the data at all energies. The lower plot shows the relative cross-section portions that arise from the four interaction categories utilized by GENIE. The relative contributions are predicted to remain in roughly constant proportion throughout the measured E_ν range, with Δ production being dominant throughout.

The squared four-momentum transfer from the lepton system, Q^2, is calculated using Eq. (5); the differential cross section, $d\sigma/dQ^2$, is shown in Fig. 15. Comparisons with GENIE, NuWro, and GiBUU-2017 predictions are presented in the upper plot, and the relative contributions from the major reaction categories as estimated by GENIE are given in the lower plot. A contribution from CC coherent scattering reaction (4) is estimated to occur in the region $Q^2 < 0.4\,\mathrm{GeV}^2$. The amount shown by the gray (dark gray) histograms in the upper (lower) plot is the rate expected from MINERvA measurements [8]. The data points in Fig. 15 include this CC coherent scattering contribution.

Even with allowance made for the presence of CC coherent scattering, the data do not exhibit a turn-over in $d\sigma/dQ^2$ as Q^2 approaches zero. The absence of a turn-over distinguishes the signal channel (1) of this work from the antineutrino and neutrino CC(π^0) channels previously studied by MINERvA [11, 13]. This may be evidence for a process similar to CC coherent scattering that populates the low Q^2 region of reactions (2) and (3), but does not participate in reactions in which the target nucleon changes its identity, such as $\bar{\nu}_\mu p \to \mu^+\pi^0 n$. Charged-current diffractive scattering on nucleons is such a process, and its presence in high energy neutrino scattering has been pointed out by D. Rein [78]. According to Rein, CC diffractive pion production must also be present in lower-E_ν scattering but its effect becomes very hard to disentangle from other CC(π) processes.

In measurements of neutrino-induced CC(π) channels carried out by MiniBooNE [79, 80] and by MINOS [81], it was found that MC agreement with data can be improved by introducing, ad hoc, a suppression of baryon-resonance production at low Q^2. This approach finds some support from Q^2-dependent reductions that ensue with theoretical treatments of nuclear medium effects that go beyond the Fermi gas model [82–86]. Figure 15 suggests that low-Q^2 suppression may not be a universal feature of charged-current pion production channels in $\nu_\mu/\bar{\nu}_\mu$ nucleus scattering.

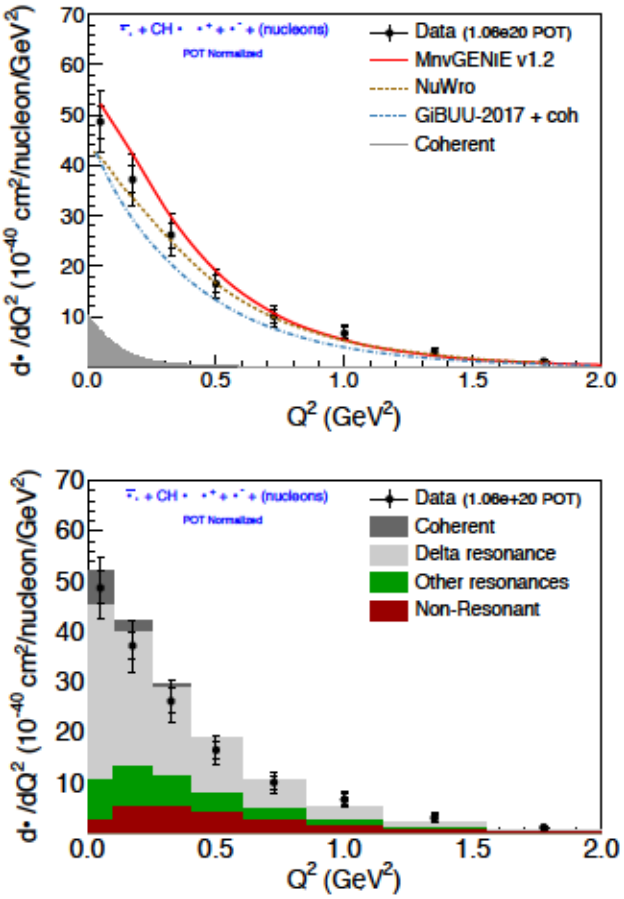

FIG. 15. Differential cross section $d\sigma/dQ^2$ for the signal channel. Upper plot: Predictions from the GENIE-based MC, NuWro, and GiBUU-2017 trend above, close to, and below the data respectively. Lower plot: Relative contributions from component processes according to GENIE. Coherent single-pion production is expected to contribute at very low Q^2.

XII. ESTIMATION OF $\bar{\nu}_\mu$-NUCLEON CROSS SECTIONS IN HYDROCARBON

The definition of signal channel (1) that the analysis has used up to this point refers to final-state topologies as they emerge from target nuclei. This signal definition is constructed such that all selections refer to directly observable quantities, and the differential cross sections subsequently presented refer to final-states that have been subjected to hadronic FSI. Cross sections in this form provide direct tests and feedback for continued

(iii) With the background and coherent scattering contributions thereby set, a fit to the vertex energy data is performed wherein the distribution shapes for reaction (2) and (3) contributions are taken from the reference simulation, and their normalizations are used as fit parameters.

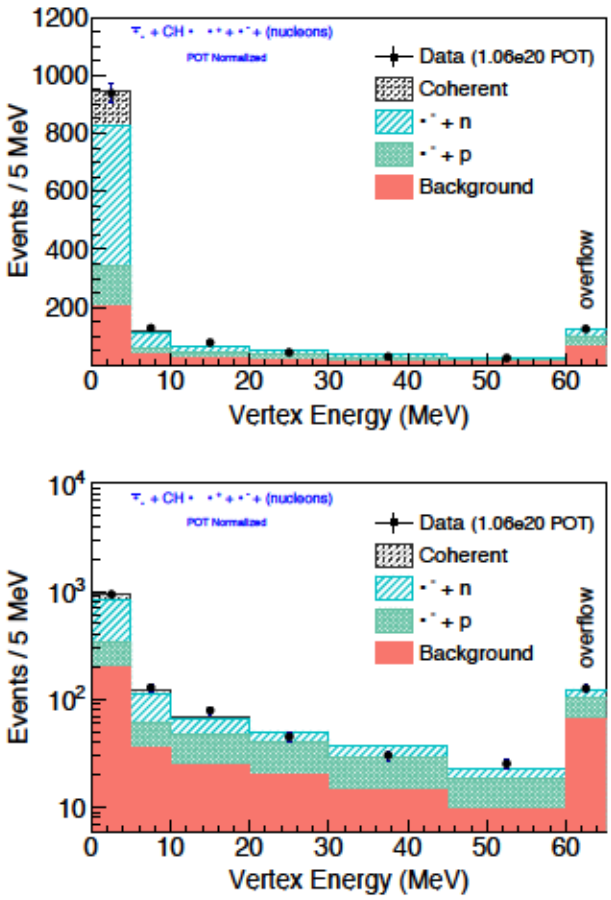

FIG. 16. Distribution of event vertex energy in the signal sample (solid circles), displayed using linear and log scales (upper, lower plots respectively). Reference MC predictions for contributions by reactions (2) and (3), labeled by their hadronic systems, are shown together with coherent scattering and background contributions. The coherent contribution is calculated from MINERvA measurement [8]; the background rate is constrained by sideband fitting, and the exclusive-reaction rates are tuned to fit the signal sample data.

It is readily seen in Fig. 16 that the fit adjustment of the MC model gives a good description of the data. Based on this description, the numbers of interactions (2) and (3) that underwrite the signal-sample population are estimated to be $N(\mu^+ n\pi^-) = 682 \pm 121$ and $N(\mu^+ p\pi^-) = 349 \pm 121$, where the error bars include systematic as well as statistical uncertainties. To convert these event counts into cross sections, it is required to know the efficiencies with which the analysis selection chain retains the progeny of reactions (2) and (3) and allows them to appear in the selected signal sample. These efficiencies, as estimated by the reference simulation, are $\epsilon(\mu^+\pi^-\mathrm{n}) = 4.9\%$ and $\epsilon(\mu^+\pi^-\mathrm{p}) = 4.1\%$. The hydrocarbon target region of MINERvA contains 15% more protons than neutrons. The difference is taken into account in order to obtain exclusive-channel cross sections that are "per nucleon" for an isoscalar target medium. The cross-section values are:

$$\sigma(\mu^+\pi^-\mathrm{n}) = 19.7 \pm 4.4 \times 10^{-40}\,\mathrm{cm}^2 \text{ per nucleon,} \quad (8)$$

$$\sigma(\mu^+\pi^-\mathrm{p}) = 12.1 \pm 4.5 \times 10^{-40}\,\mathrm{cm}^2 \text{ per nucleon.} \quad (9)$$

Comparable results are the flux-averaged cross sections for $W < 2\,\mathrm{GeV}$ based on Gargamelle antineutrino data. These are stated without errors in Table VII of Ref. [29] as follows: $\sigma(\mu^+\pi^-\mathrm{n}) = 25.1 \times 10^{-40}\,\mathrm{cm}^2$ and $\sigma(\mu^+\pi^-\mathrm{p}) = 10.1 \times 10^{-40}\,\mathrm{cm}^2$. Table 3 and Figs. 2 and 3 of Ref. [14], indicate uncertainties for these cross sections (arising from background correction, nuclear effects, and finite statistics) to be of order 25%.

XIII. ISOSPIN COMPOSITION OF $\bar{\nu}_\mu$-CC(π)

A broader perspective on $\bar{\nu}_\mu$-CC(π) reactions can be obtained by relating the MINERvA measurement of $\bar{\nu}_\mu$-CC(π^0) [10, 11] to cross sections (8) and (9). To this end, a reanalysis of the latter data has been carried out to extract the free-proton target cross section for the exclusive channel

$$\bar{\nu}_\mu + \mathrm{p} \rightarrow \mu^+ + \pi^0 + \mathrm{n}. \quad (10)$$

The measured signal channel of $\bar{\nu}_\mu$-CC(π^0) is devoid of any coherent scattering contribution, and exclusive reaction (10) is the only $\bar{\nu}_\mu$-nucleon interaction that feeds the signal channel. Consequently the extraction of the reaction (10) cross section is relatively straightforward. The event selections described in Secs. III, IV, and V are applied in the same way to the data of the earlier work. As previously noted, a weight is applied to normalize the cross section for reaction (10) to describe scattering per nucleon from an isoscalar target. The 'as born' free-nucleon target cross section for reaction (10) thereby obtained is

$$\sigma(\mu^+\pi^0\mathrm{n}) = 10.7 \pm 1.7 \times 10^{-40}\,\mathrm{cm}^2 \text{ per nucleon.} \quad (11)$$

The flux-averaged value for $W < 2\,\mathrm{GeV}$ attributed to Gargamelle [29] is $\sigma(\mu^+\pi^0\mathrm{n}) = 9.5 \times 10^{-40}\,\mathrm{cm}^2$.

The cross sections (8), (9), and (11) as hereby extracted from MINERvA data, comprise the complete set of free-nucleon cross sections for exclusive $\bar{\nu}_\mu$-CC(π) reactions. Each of these reactions proceeds via the $\Delta S = 0$ weak hadronic charged current; The current operator transforms as an isovector. This has the consequence that the final states of (2), (3), and (10) can be expressed

relative to the resonant $I = 3/2$ amplitude, and indicate the two amplitudes to be 90° out of phase on average.

Experiment medium	ν flux [GeV]	W [GeV]	R^ν	ϕ^ν degrees
Gargamelle[15]	~0.5 - 10.0	≤ 1.4	0.71±0.14	$75^{+12°}_{-16°}$
propane-freon	peak: 1.5	all data	1.03±0.15	$73^{+12°}_{-10°}$
BNL 7' BC[87]	< 3.0	≤ 1.4	0.60±0.07	90±11°
deuterium	peak: 1.0	≤ 1.6	0.79±0.05	95±7°
		all data	0.89±0.05	97±6°
ANL 12' BC[88]	< 1.5	≤ 1.4	0.68±0.04	90.7±4.6°
deuterium	peak: 0.5	≤ 1.6	0.75±0.04	92.0±4.1°

TABLE II. Neutrino bubble chamber measurements of relative strength and phase for the isospin 1/2 and 3/2 amplitudes of neutrino-induced $CC(\pi)$ production. Values obtained for neutrino-induced R^ν and ϕ^ν are similar to those reported in Table I for antineutrino single-pion production.

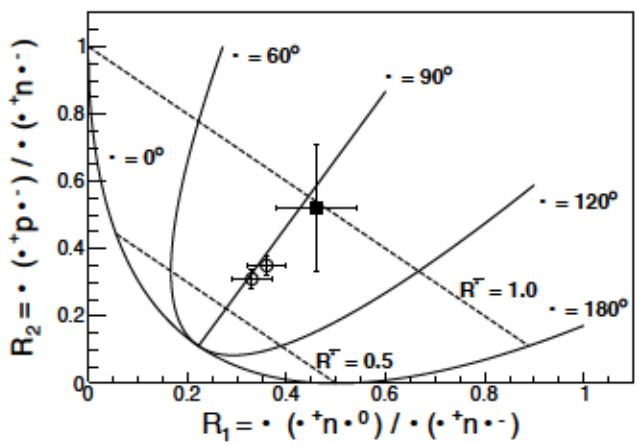

FIG. 17. Plot of the cross-section ratios R_2 versus R_1 for selected $\bar{\nu}_\mu$ and ν_μ data. Dashed lines denote constant values of $|A_1|/|A_3|$ and solid-line curves denote values of the relative phase. The MINERvA measurements (solid square), as with Gargamelle (not plotted; see Table I) show that A_1 and A_3, averaged over a wide-band $\bar{\nu}$ flux, are of similar strength and devoid of interference. Results obtained with ν_μ-CC(π) reactions (open circles, from overlapping samples) indicate $|A_3| > |A_1|$ in neutrino samples at lower incident energies and lesser reach in W [88].

A discernible trend in the neutrino results is that higher reach in W correlates with larger R^ν values. This is understandable because, above $W > 1.4$ GeV, the $\Delta(1232)$ contribution is diminished while $I = 1/2$ baryon resonances gain strength. The MINERvA data contain a relatively large contribution from events with W between 1.4 - 1.8 GeV compared to the ANL and BNL data sets, and this may be the reason why $R^{\bar{\nu}}$ of MINERvA is larger than R^ν as measured by ANL and BNL.

A convenient way to compare measurements of the relative magnitude and phase of A_1 versus A_3 is with the diplot shown in Fig. 17. The plot maps measurements of the cross-section ratios R_1 and R_2 onto a coordinate grid of slanted dashed lines and solid-line curves that denote values of $R^{\bar{\nu}}$ and $\phi^{\bar{\nu}}$ respectively. The MINERvA and Gargamelle antineutrino measurements lie within 1σ of $(R^{\bar{\nu}}, \phi^{\bar{\nu}}) \simeq (1.0, 90°)$, indicating the amplitude strengths to be nearly equal and non-interfering ($\cos\phi^{\bar{\nu}} \simeq 0$). The neutrino measurements, working with lower-W samples, also lie along the $\phi = 90°$ axis but at R^ν values distinctly less than 1.0. The plot suggests that the representation point for a CC(π) sample migrates upward along $\phi^\nu = 90°$), as the average W of the sample is increased.

XIV. CONCLUSIONS

A study of semi-exclusive $\bar{\nu}_\mu$-CC(π^-) scattering on hydrocarbon is reported using $\bar{\nu}_\mu$ interactions with $E_{\bar{\nu}}$ ranging from ~ 1.5 to 10 GeV, with final-state $W < 1.8$ GeV. This is the first experiment working in the few-GeV region of incident $\bar{\nu}_\mu$ to report differential cross sections for μ^+ and π^- kinematic variables θ_μ, p_μ, T_π, and θ_π, while also reporting cross sections as functions of $E_{\bar{\nu}}$ and Q^2. Data summary tables for these measurements that may facilitate phenomenological investigations are available in the Supplement [75].

Measured differential cross sections are compared to predictions based upon the GENIE, NuWro, and GiBUU-2017 event generators. The predictions generally reproduce the shapes of the differential cross sections, with $d\sigma/d\theta_{\pi^-}$ being the sole exception. The event generators differ with respect to predictions for absolute event rate. The GENIE-based simulation gives the highest event rate and its prediction exceeds the observed data rate by 8%.

The shape of the pion T_π differential cross section is considered in light of GENIE's effective cascade treatment of processes that comprise pion FSI. The modeling provides a detailed picture for the $d\sigma/T_\pi$ distribution that is consistent with the data (Fig. 12). This same picture suggests that adjustments to pion FSI elastic and inelastic scattering that promote emission into smaller, more forward angles may be in order (Fig. 13). For $d\sigma/dQ^2$, neither the data nor the generator curves exhibit a turn-over in the distribution at very-low Q^2. This observation contrasts with distribution turn-over for $Q^2 < 0.20$ GeV^2 that occurs in MINERvA measurements for $\bar{\nu}_\mu$-CC(π^0) [10] and ν_μ-CC(π^0) channels [11, 13].

The signal sample has been decomposed into $\bar{\nu}_\mu$ interactions of four kinds, with exclusive reactions (2) and (3) being the major contributors. Flux-averaged quasi-free nucleon scattering cross sections are presented in Eqs. (8) and (9). The flux-averaged cross section (11) is extracted from the published MINERvA mea-

et al. *et al.*

et al.

et al.

et al.

et al. *et al.*

et al. *et al.*

et al.

et al.

et al.

et al.

et al.

et al.

et al.

et al.

et al.

et al.

et al.

et al.

et al.
et al.
et al.
et al.
et al.
et al.
et al.
et al.
et al.
et al.
et al.
et al.
et al.
et al.
et al.
et al.
et al.
et al.
et al.
et al.
et al.
et al.
et al.
et al.
et al.
et al.